Nonequilibrium Electron-Phonon and Electron-Ion Couplings in Warm Dense Copper

Gyeongbo Kang[1,2,†], Gyusang Lee[1,†], Sam Azadi[3], Robert Carley[4], Loïc Le Guyader[4], Le Phuong Hoang[4], Han Byul Kim[1], Minju Kim[5], Changhoo Lee[1], Laurent Mercadier[4], Giuseppe Mercurio[4], Sergii Parchenko[4], Ahhyun Seong[1], Dongbin Shin[1], Martin Teichmann[4], Benjamin E. Van Kuiken[4], Zhong Yin[4], Sam M. Vinko[3,6], Andreas Scherz[4], Byoung Ick Cho[1,*]

[1]*Department of Physics and Photon Science, Gwangju Institute of Science and Technology, Gwangju 61005, Republic of Korea*

[2]*Pohang Accelerator Laboratory, Pohang, Gyeongbuk 37673, Republic of Korea*

[3]*Department of Physics, University of Oxford, Oxford OX1 3PU, United Kingdom*

[4]*European XFEL, Schenefeld 22869, Germany*

[5]*Frontier of Extreme Physics, Interdisciplinary Materials Measurement Institute, Korea Research Institute of Standards and Science, Daejeon 34133, Republic of Korea*

[6]*Central Laser Facility, STFC Rutherford Appleton Laboratory, Didcot OX11 0QX, United Kingdom*

[*]E-mail: bicho@gist.ac.kr

[†]*These authors contributed equally to this work.*

Abstract:

Electron-phonon and electron-ion coupling dynamics in warm dense copper are investigated using femtosecond time-resolved X-ray absorption near-edge structure spectroscopy at the Cu L_3 edge. Measurements performed with 0.5 eV spectral and 100 fs temporal resolutions reveal pronounced transient changes in pre-edge absorption, indicating strong nonequilibrium behavior in the electronic system. By comparing experimental spectra with simulations based on a modified two-temperature model coupled with density functional theory-calculated density of states, the temporal evolution of coupling strength is quantified across solid and liquid phases. Nonequilibrium electron distributions are found to significantly enhance electron-phonon coupling in the solid phase due to broadened electron energy distributions immediately following laser excitation. Upon melting, the coupling becomes

weaker and less sensitive to electron distributions, reflecting a transition to a more disordered atomic structure and increasingly thermalized electrons. These experimental observations are accurately reproduced by theoretical modeling that explicitly incorporates electron relaxation dynamics. The critical role of nonequilibrium electron kinetics in understanding ultrafast energy transfer processes in laser-excited materials is thus highlighted, providing benchmark data essential for future modeling of material behavior under extreme conditions.

1. Introduction

The interaction of high-intensity femtosecond laser pulses with thin metal foils provides a well-controlled platform for driving matter into extreme thermodynamic states [1-4]. Upon irradiation, conduction electrons in the metal rapidly absorb the laser energy, while the heavier lattice remains cold for several hundred femtoseconds. This leads to a strong electron-lattice nonequilibrium condition and, under appropriate fluence, drives the system into the regime of warm dense matter (WDM)—a unique state characterized by solid-like densities, temperatures of 10^4–10^6 K, partial ionization, and strong interparticle coupling [5-7].

Understanding WDM is of fundamental and technological importance. It occurs naturally in astrophysical environments such as the interiors of giant planets and brown dwarfs, and plays a central role in laboratory settings including inertial confinement fusion, laser shock compression, and ultrafast materials processing [8-11]. Despite its relevance, WDM remains one of the least understood phases of matter, due to its transient nature and the difficulty of modeling its thermophysical properties with conventional solid-state or plasma physics approaches.

A key physical quantity in WDM is the rate of energy exchange between electrons and ions, often described by a coupling parameter G. This rate governs the dynamics of melting, structural relaxation, and the onset of hydrodynamic motion in laser-heated materials [12-14]. Accurately determining this coupling strength is crucial for predictive modeling of laser-matter interaction, including applications such as ablation, surface modification, and material phase control.

Previous experimental efforts have attempted to probe electron-lattice coupling in WDM, notably using picosecond-resolved X-ray absorption near-edge spectroscopy (XANES) in copper and ultrafast electron diffraction in gold [15, 16]. While these studies provided valuable data in the picosecond regime, they were typically limited to timescales beyond the initial excitation, where the electron system had already begun to thermalize. In addition, the presence of mixed-phase states during melting complicated the interpretation of the coupling dynamics.

More recently, femtosecond XANES measurements using XFEL have revealed the presence of nonthermal electrons with characteristic lifetimes on the order of several hundred femtoseconds, as well as a pronounced downshift of the *d*-band arising from the formation of holes in the Cu *d*-band [17, 18]. These findings suggest that high-quality data capturing

nonequilibrium electronic states are essential to adequately describe the ultrafast thermodynamic processes in warm dense copper. It is also noted that References [19, 20] presented detailed XANES measurements of warm dense copper and analyses of lattice disorder during melting processes with picosecond temporal resolution. However, these studies assumed that the electronic system was in thermal equilibrium and did not address the possible effects of nonthermal electron distributions during the early femtosecond regime immediately following excitation.

On the theoretical side, many models estimate coupling strength by interpolating between solid-state and plasma-based formalisms [21, 22]. While computationally convenient, these interpolations lack microscopic justification in the WDM regime. More rigorous approaches using density functional theory (DFT) have offered improved predictions, but their outcomes remain highly sensitive to assumptions about electronic structure, lattice configuration (solid vs. liquid), and whether electrons are in thermal equilibrium [23-31]. Notably, DFT-based studies of coupling strength often show significant variability under nominally similar conditions, indicating the need for direct experimental validation.

In this study, we combine femtosecond-resolved XANES measurements with nonequilibrium modeling to investigate energy relaxation dynamics in laser-heated copper foils. By probing the Cu L_3 edge with sub-100 fs resolution at the European XFEL, we capture the transient evolution of the electronic structure and absorption features as the system evolves from solid to liquid. To interpret these results, we implement a modified two-temperature model (m-TTM) that incorporates time-dependent nonequilibrium electron distributions and DFT-calculated electronic density of states for both phases. Our results reveal that nonthermal electrons significantly enhance the coupling strength in the solid phase, while in the liquid phase, the coupling becomes weaker and less temperature-dependent. These findings are supported by our theoretical calculations and match the experimental trends, providing phase-resolved, time-dependent insight into electron-lattice energy exchange in WDM. This study establishes a benchmark for coupling measurements in laser-heated matter and contributes to the development of predictive models for ultrafast surface and material response under extreme conditions.

2. Experiment

The XANES spectra of the laser-heated Cu were measured using the transient absorption spectroscopy apparatus of the Spectroscopy and Coherent Scattering (SCS) instrument of the European XFEL. A schematic and the detailed description of the experimental setup can be found in Ref. [32]. The sample was a free-standing 40 ± 5 nm polycrystalline Cu foil coated with 10 ± 2.5 nm SiO_2 on both sides to prevent oxidation. The target was pumped with a 50 fs laser pulse at 400 nm wavelength and an incident fluence of 150 mJ/cm^2. Independent measurements of the reflection and transmission of the laser pulse indicated that the corresponding absorbed energy density was E_d = 2.39 ± 0.12 MJ/kg. It is noted that under this laser fluence, single-photon absorption remains the dominant process for SiO_2 (bandgap ~9 eV), and the coating remained largely transparent. In addition, given that the speed of shock or heat propagation in the sample is on the order of 10^4 m/s, significant hydrodynamic motion of the entire target would start at approximately 60 nm / (10^4 m/s) ≈ 6 ps. Since the majority of the measurements were performed before this timescale, hydrodynamic expansion and any associated effects from the SiO_2 layer are expected to be minimal. After each laser pulse, the damaged sample was translated to a fresh area.

The transmission and absorption of the XFEL probe through the laser-heated Cu were measured around the L_3 edge with an energy resolution of 0.5 eV and a time resolution of 100 fs. The transmitted X-ray pulses were detected with the pulse-resolved DSSC detector [33]. Each data point was averaged over approximately 30 laser shots and the typical standard deviation of the data was about 3 %. Fig. 1 shows the spectra obtained at various pump-probe delays. The spectrum at a negative delay displays the L_3 edge and near-edge structure of ambient copper, with low pre-edge absorption indicating a fully occupied 3*d*-band.

Following laser excitation, the spectra reveal a strong increase in pre-edge absorption at 100 fs, with a peak appearing at 929.5 eV. This feature is attributed to the creation of holes near the top of the 3*d*-band, indicating a downward shift of the band. Such a shift can be understood in terms of reduced screening of the electron-ion potential in the excited 3*d*-band [18, 34]. For comparison, Fig. 1 shows spectra calculated based on the time-dependent high-temperature Fermi distribution derived from the conventional two-temperature model (TTM) (black dashed curves) as well as spectra obtained using the nonequilibrium electron distribution (blue curves), which will be further discussed in the later sections. The details of TTM-based calculation have been presented in previous works [17, 35]. Notably, the experimentally observed absorption peaks are both larger in magnitude and shifted to lower energies compared to the TTM simulations. It is also interesting to compare these new data with other femtosecond

XANES measurements [18, 36]. In Ref. [36], 4*sp* electrons are pumped with infrared photons, and the excited 4*sp* electrons subsequently interact with the 3*d*-band. In Ref. [18], X-rays promote 2*p* core electrons directly above the Fermi level. The 3*d* electrons then decay into the excited core holes via cascade Auger processes and are refilled by 4*sp* electrons. In both cases, the 3*d* electrons do not directly interact with the incident photons.

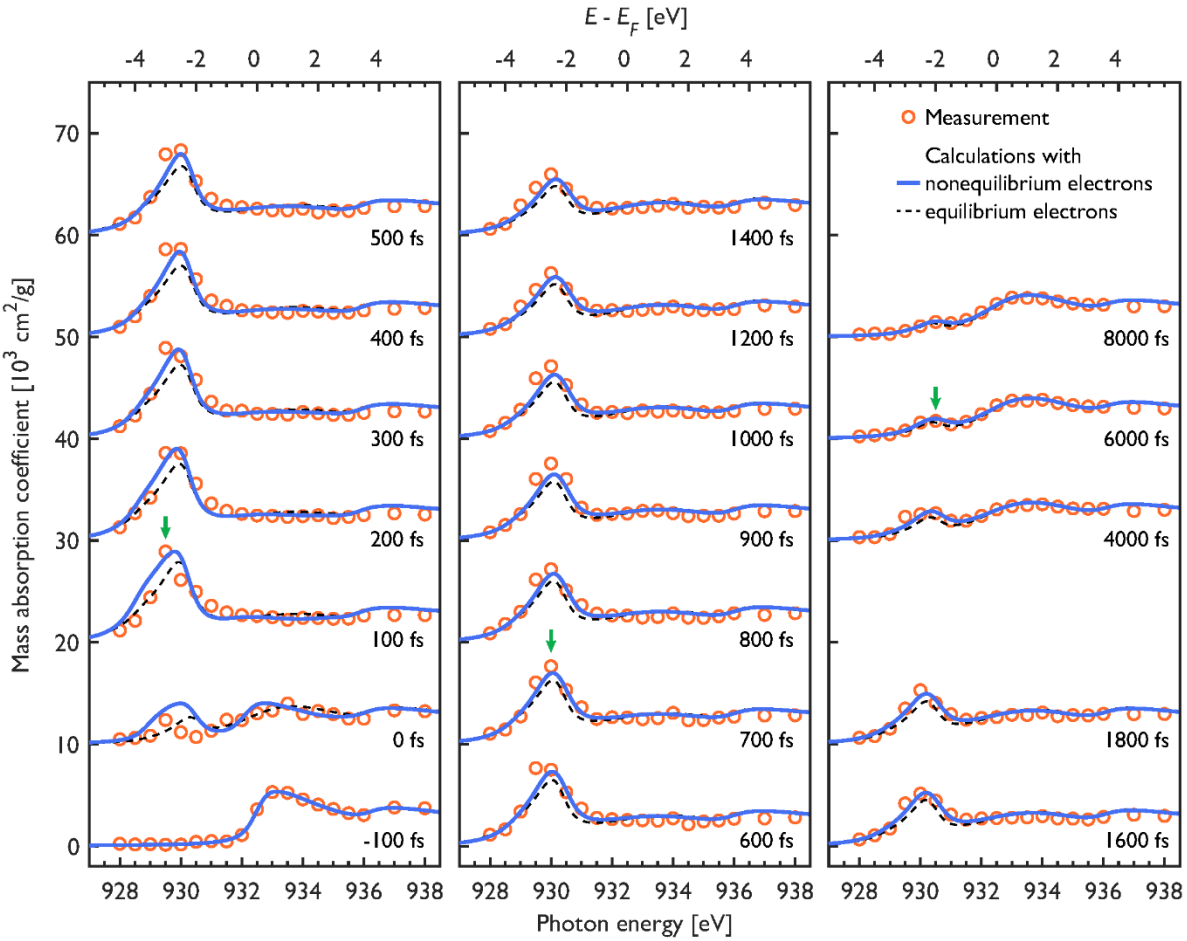


Fig. 1. Evolution of L_3 XANES spectra of laser-heated Cu (red circles). Green arrows indicate pre-edge absorption peaks at E-E_F = -2.75, -2.25, and -2 eV. Spectra are compared to high-temperature absorption spectra calculated using nonequilibrium electron model (blue curves) and equilibrium electron model (black dashed curves). Each spectrum is vertically offset by 10,000 cm²/g for clarity.

Over the next several hundred femtoseconds, this peak shifts to higher energy, reflecting the refilling of the 3*d*-band and the gradual recovery dynamics. Beyond 700 fs and up to 2 ps, the peak stabilizes near 930 eV while the overall pre-edge absorption diminishes. Even in this time regime, the calculated XANES spectra with equilibrium electrons, based on the conventional TTM approach (black dashed curves), systematically underestimate the

overall pre-edge absorption. In contrast, calculations incorporating nonequilibrium electron distributions (blue curves) show much better agreement with the experimental measurements. These observations in the early time regime highlight the critical influence of nonequilibrium electron distributions on the X-ray absorption features, which cannot be fully described using equilibrium models alone.

To quantify the degree of nonequilibrium, we define a difference signal between the measured and the TTM-based calculation spectra below the Fermi energy and fit its temporal evolution to an exponential decay. As shown in Fig. 2, this fit yields a characteristic time of approximately 1.6 ps, which is consistent with the lifetime of nonthermal electron distributions reported in a prior study [17], although the data quality in that work limited a more robust quantitative analysis.

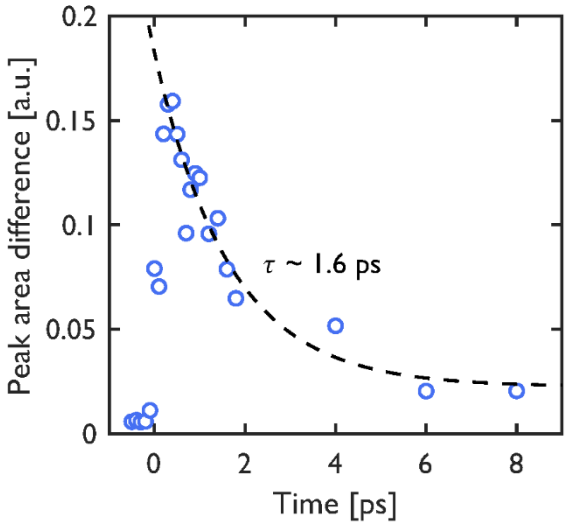


Fig. 2. Temporal evolution of the absorption difference below the Fermi level between the measured and calculated spectra shown in Fig. 1. The data are fit to an exponential function, yielding a characteristic decay time of 1.6 ps.

3. Modeling

3.1. Modified two-temperature model (m-TTM)

To gain further insight into the dynamical processes, we employ the following model for nonequilibrium WDM. The evolution of the energy densities in the electronic and ionic

subsystems is governed by the following set of coupled equations:

$$\frac{\partial U_e}{\partial t} = -G\left(\frac{U_e}{c_e} - T_l\right) + S(t), \quad (1)$$

$$\frac{\partial U_l}{\partial t} = G\left(\frac{U_e}{C_e} - T_l\right). \quad (2)$$

U, T, and S represent the internal energy density, temperature, and absorbed laser power density, respectively. The subscripts e and l denote the electrons and lattice, respectively. G is the electron-phonon (or electron-ion) coupling parameter.

These equations follow the structure of the conventional TTM. However, to describe a nonequilibrium electron distribution in which the temperature is not well-defined, the electron temperature is replaced with U_e/C_e. $U_e = \int gf\ \varepsilon d\varepsilon - U_e^0$ is the internal energy, C_e is electron heat capacity, and g, f, and U_e^0 are the total density of states (DOS), electron distribution function, and the ground state energy, respectively [37].

It should be noted that while we aim to emphasize the role of nonequilibrium effects, the overall framework is still grounded in thermodynamic concepts developed under equilibrium conditions. C_e is inherently defined as the derivative of internal energy with respect to electron temperature, and in principle it cannot be rigorously defined without introducing some notion of temperature. Similarly, the electron-phonon coupling parameter has units of energy density per unit time per unit temperature, which also requires specifying a temperature. Therefore, in this work, we introduce an effective temperature that corresponds to the Fermi distribution associated with the calculated U_e. This quantity is only employed in those parts of the model where it is strictly necessary to incorporate thermodynamic parameters.

This m-TTM framework allows us to simulate the nonequilibrium energy exchange between electrons and lattice in both solid and liquid phases. The model is coupled to time-resolved X-ray absorption spectra, providing a direct link between microscopic electronic dynamics and experimentally observable quantities.

3.2. Electronic density of states

The electronic density of states (DOS) plays a critical role in determining the energy absorption and relaxation behavior in warm dense copper. We calculate the DOS for both the solid and liquid phases of Cu at density of 8.9 g/cm^3 with excited valence electrons using

density functional theory (DFT) as implemented in the QUANTUM ESPRESSO package [38]. The Optimized Norm-Conserving Vanderbilt (ONCV) pseudopotentials are employed [39, 40], and a plane wave cutoff is up to 80 Ry. The Perdew-Berke-Ernzerhof (PBE) exchange-correlation functional is adopted to describe electron-electron exchange and correlation [41]. For solid Cu, a 20 × 20 × 20 Monkhorst-Pack *k*-point grid is implemented to sample the Brillouin zone [42]. To mimic the liquid phase under the periodic boundary conditions, *ab initio* molecular dynamics (AIMD) calculation is performed at 3000 K using the 3 × 3 × 3 supercell containing 108 Cu atoms. A 2 × 2 × 2 *k*-point grid is used to sample the Brillouin zone for this extended supercell. The time step for the AIMD is set to 4.8 fs, and we calculate the average DOS of each structure for different electron temperatures (0.026 eV, 1 eV, and 2 eV) with enough sampled snapshots among the trajectories. It is noted that the ionic temperature has a negligible influence on the liquid DOS because the displacement of ions is averaged out over multiple configurations.

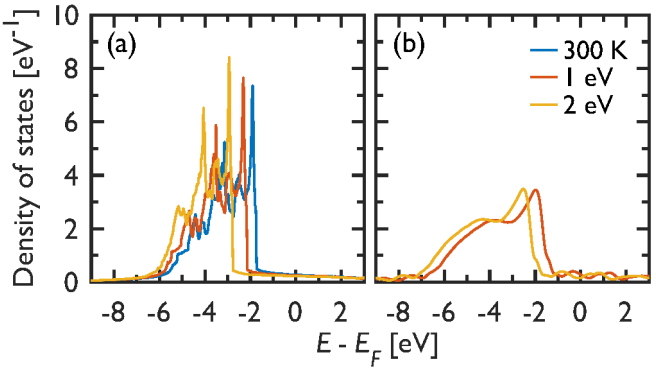


Fig. 3. Calculated density of states for (a) solid (T_I = 300 K) and (b) liquid (T_I = 3000 K) copper with various electron temperatures.

As shown in Fig. 3, increasing the electronic excitation leads to the depopulation of the Cu 3*d*-band in both phases. This depopulation reduces the screening effect of the *d* electrons, resulting in a downward shift of the *d*-band energy levels. Notably, the depopulation of *d* electrons can occur not only due to elevated electronic temperatures but also due to direct optical excitation from the pump laser. Therefore, the time evolution of the DOS must be updated self-consistently in each time step, reflecting both the distribution function and the 3*d*-band population. This dynamic behavior of the DOS provides a microscopic basis for understanding the transient changes observed in XANES spectra. In our simulations, we use the solid-phase DOS up to 500 fs, after which the system is assumed to have melted, and the

liquid-phase DOS is used for subsequent times. This time threshold is supported by the evolution of the lattice energy in our experimental analysis (see Section 4).

3.3. Equilibration of nonthermal electrons

To account for the nonequilibrium nature of the excited electronic system, we separate the electron distribution function into thermal and nonthermal components [43-45]:

$$f = f^{TH} + f^{NT} \tag{3}$$

where f^{TH} follows the Fermi-Dirac distribution, and f^{NT} describes the nonthermal part resulting from direct excitation. The evolution of f^{NT} is modeled by the following kinetic equation:

$$g \cdot f^{NT}(\varepsilon, t + dt) = \alpha \cdot P(\varepsilon, t)\, dt + g \cdot f^{NT}(\varepsilon, t)\, e^{-\frac{dt}{\tau}}, \tag{4}$$

The function P represents the net photon-induced excitation by photons $\hbar\omega$ within the envelope g, generating the nonthermal distribution.

$$\begin{aligned} P(\varepsilon) = {} & g(\varepsilon - \hbar\omega) f(\varepsilon - \hbar\omega)\, g(\varepsilon)[1 - f(\varepsilon)] \\ & - g(\varepsilon) f(\varepsilon)\, g(\varepsilon + \hbar\omega)[1 - f(\varepsilon + \hbar\omega)]. \end{aligned} \tag{5}$$

This process is proportional to the density of initially occupied and final unoccupied states, resulting in negative and positive contributions at low and high energy ranges, respectively. The coefficient α in Eq. (4) is set to ensure energy conservation at each time, satisfying $\partial U_e = \int g(\partial f^{NT} + \partial f^{TH})\, \varepsilon d\varepsilon \approx S(t)dt$. It is an approximation of Eq. (1). During laser irradiation, a typical power transferred to the lattice ($G\Delta T \approx 10^{21}$ W/m^3) is negligible compared to the absorbed laser power ($\sim 10^{24}$ W/m^3).

The decay of f^{NT} is described using a characteristic time scale given by the following expression.

$$\bar{\tau} = \langle \int \tau(\varepsilon) f^{NT}(\varepsilon) d\varepsilon \rangle \tag{6}$$

where the energy-dependent lifetime of nonthermal electrons is given by $\tau(\varepsilon) = \tau_0\mu^2/((\varepsilon-\mu)^2 + (\pi T_e^{TH})^2)$ [44]. Electrons near the chemical potential μ have longer lifetime than those farther away. Here, μ is updated dynamically at each time step to remain consistent with the evolving nonthermal electron distribution. By calculating the expectation value $\bar{\tau}$ and choosing τ_0 = 160 fs, the resulting characteristic decay time is found to be approximately $\bar{\tau} \sim$ 1.6 ps, consistent with the experimental result shown in Fig. 2.

Fig. 4 illustrates the time evolution of the electronic system, showing (i) the DOS, (ii) the nonthermal distribution multiplied by DOS $g{\cdot}f^{NT}$ and (iii) the thermal component f^{TH}. For times earlier than 500 fs, the solid-phase DOS from Fig. 3(a) is used, while for later times, the liquid-phase DOS from Fig. 3(b) is applied. This model forms the basis for calculating the time-dependent internal energy $U_e(t)$, which is then used in the m-TTM (see Section 3.1) to simulate the coupled evolution of the electron and lattice systems. By explicitly treating the nonthermal component, we capture transient energy redistribution processes that strongly influence the coupling strength.

It is noted that there have been different approaches to describing nonequilibrium electron kinetics. For example, recent work by Held *et al.* introduced nonequilibrium band occupation between the *d*- and *sp*-band in noble metals [46]. Although the specific implementations differ in detail, as shown in Fig. 4(b), our model similarly predicts a redistribution of electrons, with reduced occupancy in the *d*-band and increased occupancy in the *sp*-band, resulting in a broader energy spread. Therefore, similar effects on thermodynamic properties are expected.

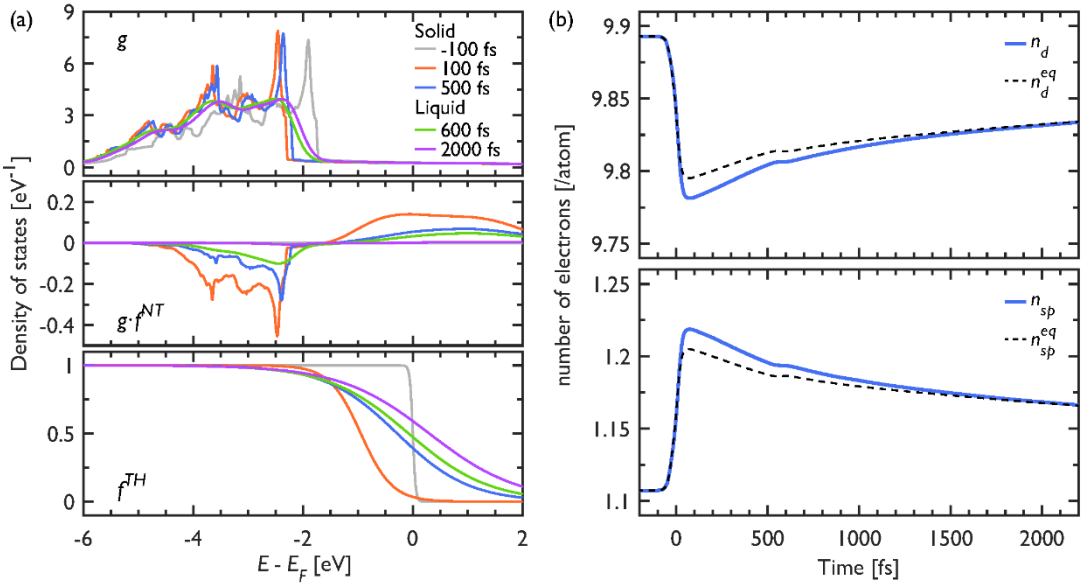


Fig. 4. (a) Temporal evolution of (top) Cu DOS, (middle) nonthermal electron distribution multiplied by DOS $g \cdot f^{NT}$, and (bottom) thermal electron distribution f^{TH}. (b) Occupation in the *d*-band (top) and the *sp*-band (bottom). Band occupation corresponding to the Fermi distributions are shown as black dashed curves.

4. Electron-phonon and Electron-ion couplings

4.1. Experimental determination

To quantify the electron-phonon and electron-ion coupling strength, we extract the coupling parameter G_{exp} by comparing measured XANES spectra (Fig. 1) with simulated spectra based on the nonequilibrium m-TTM framework described in Section 3. The strategy involves iteratively adjusting the coupling value in the simulations to ensure that the resulting absorption spectra match the experimental data at subsequent pump-probe delays. Specifically, we solve the coupled equations for the electron distribution (Eqs. (3–5)) and internal energy (Eqs. (1–2)) over a series of time steps, using trial values of G. For each delay, we select the G_{exp} that best reproduces the measured XANES spectrum at the subsequent time step. For instance, the value of G_{exp} at 100 fs is chosen such that the calculated spectrum at 200 fs matches the corresponding experimental measurement.

Fig. 5(a) presents examples of the detailed fitted XANES spectra, corresponding to the data already shown in Fig. 1. For both the solid and liquid phases, the calculated spectra using the nonequilibrium electron distribution and the experimentally determined coupling parameter G_{exp} (blue curves) show significantly improved agreement with the measured data compared to those obtained using the conventional TTM-based calculation with $G_{cal}(\tau = 0 \text{ ps})$ (gray curves). In particular, at 200 fs when the nonthermal electron population is most dominant, the calculated pre-edge absorption peak closely reproduces both the height and spectral position observed in the experiment. This agreement is especially notable at early delays, where strong nonequilibrium conditions cause a downward shift in the depopulated Cu 3*d*-band (see Fig. 3(a)), a feature that is captured by our modeling. Detailed methods for calculating the Cu L_3 XANES spectra are described in references [47, 48].

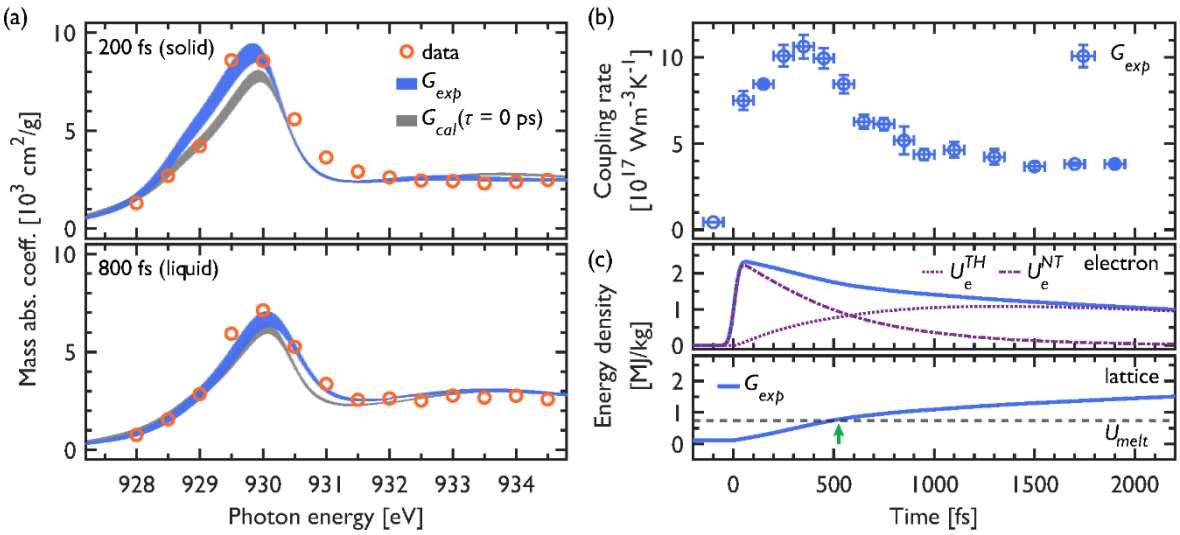


Fig. 5. (a) Comparison of XANES spectra at selected times (red circles) with spectra calculated using G_{exp} (blue curves) and $G_{cal}(\tau = 0\,ps)$ (gray curves). The thickness of the curves represents the uncertainty in the calculation arising from experimental errors, such as the absorbed laser energy density. (b) Experimentally determined G_{exp} values at different times. (c) Temporal evolution of energy density for (top) electrons and (bottom) the lattice, calculated using G_{exp} (blue curve). The temporal evolution of the energy densities for thermal (U_e^{TH}) and nonthermal (U_e^{NT}) electrons are shown as purple dotted and dashed-dotted curves, respectively. The lattice energy density corresponding to the melting threshold U_{melt} is indicated with a black dashed line. The green arrow marks the time at which the lattice energy density reaches U_{melt}.

Fig. 5(b) show the corresponding G_{exp} values determined based on the XANES fit in Fig. 5(a). The extracted coupling strengths G_{exp} are substantially enhanced during the first 500 fs, reaching values approximately an order of magnitude larger than the equilibrium value of 10^{17} Wm^{-3}K^{-1} reported for room-temperature Cu [49]. This enhancement arises from the broad nonequilibrium electron distribution (shown in Fig. 4), which increases the phase space available for energy exchange with phonons. Interestingly, the coupling peaks around 400 fs, even though the nonthermal distribution f^{NT} is less pronounced than at earlier times. This suggests that both thermal and nonthermal components contribute to the enhancement, with the thermal component f^{TH} becoming broader and more active during this regime compare to earlier times. The combined effects of both components are illustrated in Fig. 4(b). During this period, the band occupations deviate from equilibrium conditions, characterized by reduced occupancy in the *d*-band and increased population in the *sp*-band. Notably, this behavior is also consistent with recent calculations for nonequilibrium noble metal systems such as gold [46], which emphasized the role of chemical potential shifts in enhancing electron-phonon coupling.

Fig. 5(c) shows the corresponding temporal evolution of U_e and U_l. At around 500 fs, the lattice energy density surpasses the melting threshold U_{melt}, marking the onset of melting. From this point forward, the electronic structure and coupling are treated using liquid-phase DOS (see Fig. 3(b)). The experimentally extracted coupling rate decreases and stabilizes at approximately 4–5 × 10^{17} $Wm^{-3}K^{-1}$. This behavior indicates that, in the liquid phase, the coupling becomes less sensitive to temperature and is dominated by thermalized electrons. The gradual reduction in G_{exp} further suggests that the nonthermal component plays a reduced role beyond 1 ps, as the system approaches thermal equilibration.

4.2. Theoretical calculations

To further validate the experimentally extracted coupling strengths and understand their physical origins, we performed theoretical calculations of electron-phonon (solid) and electron-ion (liquid) coupling using a microscopic formalism based on the electronic structure and distribution functions. These calculations allow for direct comparison with models that explicitly incorporate nonequilibrium effects, providing deeper insight into the mechanisms governing energy relaxation in warm dense copper.

The coupling strength G is computed using the following equation:

$$G = G_0 \int \frac{g^2(\varepsilon)}{g^2(\mu)} \left(-\frac{\partial f}{\partial \varepsilon}\right) d\varepsilon, \tag{7}$$

This expression is derived from the Bloch-Boltzmann-Peierls framework [50] and later reformulated by Allen [51], Wang *et al*. [52], and Lin *et al.* [23].

For the solid phase, G_0 denotes the electron-phonon coupling at 0 K and is expressed as $G_0^{solid} = \pi\hbar k_B \lambda \langle\omega^2\rangle g(\epsilon_F) = 4.376 \times 10^{16}$, where λ and $\langle\omega^2\rangle$ are electron-phonon mass enhancement factor and the second moment of the phonon spectrum, respectively [23]. For the liquid phase, we adopt an expression from Simoni *et al*. [53], where $G_0^{liquid} = |f_{Ix}|^2 g(\epsilon_F)^2 =$ (3.97–2.30) × 10^{16} in 0.5–1 eV range, and f_{Ix} is the matrix elements for interaction between ion and a Kohn-Sham electron.

By solving Eqs. (1–4) in a fully self-consistent manner, we evaluate the time-dependent coupling strength G_{cal} for both nonequilibrium (τ = 1.6 ps) and equilibrium (τ = 0 ps) electron distributions. In this calculation, the electron distribution evolves dynamically, and

the transition from solid to liquid phase is implemented by switching both the DOS and G_0 when the lattice energy exceeds the melting threshold U_{melt}.

Fig. 6 shows the results of these calculations together with experimentally extracted values G_{exp} for comparison. The red curve corresponds to $G_{cal}(\tau = 1.6\,\text{ps})$, computed with a nonequilibrium electron distribution incorporating a decay time for nonthermal electrons, while the black dashed curve shows $G_{cal}(\tau = 0\,\text{ps})$, which assumes instantaneous thermalization. Both calculated curves are convoluted with the 100 fs experimental time resolution.

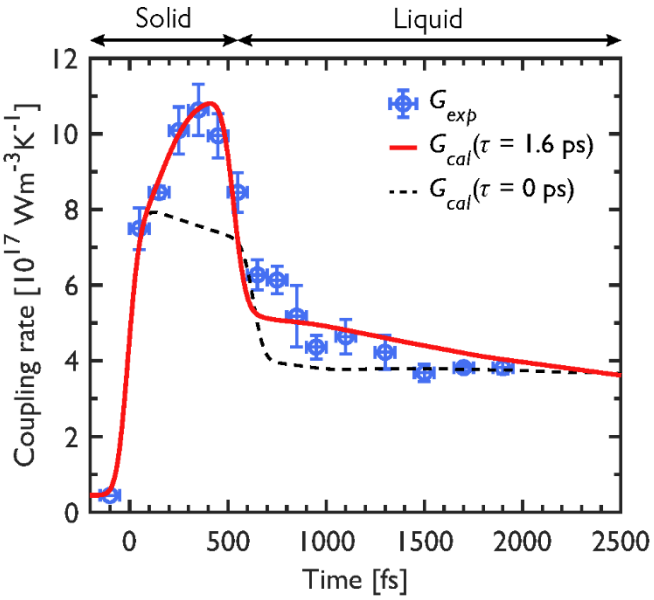


Fig. 6. Temporal evolution of the electron-phonon/electron-ion coupling strength calculated with a nonequilibrium electron distribution (G_{cal} (τ = 1.6 ps), red) and with a fully equilibrated electron distribution (G_{cal}(τ = 0 ps), black). Both theoretical results are convolved with the 100 fs temporal resolution of the measurements. Experimentally extracted values (G_{exp}, blue) are overlaid for comparison.

In the solid phase (t < 500 fs), $G_{cal}(\tau = 1.6\,\text{ps})$ agrees well with G_{exp}, indicating that the enhanced coupling is primarily driven by nonequilibrium electron distributions. These nonequilibrium distributions, broadened by strong optical excitation, expand the phase space available for scattering, thereby accelerating energy transfer to the lattice. In contrast, the equilibrium model $G_{cal}(\tau = 0\,\text{ps})$ significantly underestimates the coupling, demonstrating that thermalized electrons alone cannot account for the observed rates.

After melting begins, the $G_{cal}(\tau = 1.6\,\text{ps})$ decreases sharply due to the transition to the liquid-phase DOS and corresponding G_0 reflecting the reduced coupling efficiency in the disordered atomic environment. In the liquid phase (t > 700 fs), a similar trend is observed: both $G_{cal}(\tau = 1.6\,\text{ps})$ and G_{exp} remain higher than $G_{cal}(\tau = 0\,\text{ps})$, indicating nonequilibrium

electrons still play a role in enhancing the coupling rate. However, notable differences also arise. The overall electron-ion coupling strength is lower than that for electron-phonon coupling, and it reaches a relatively constant value after 1 ps, even as the electron and ion temperatures continue to evolve, as shown in Fig. 5(c). This behavior suggests that electron-ion coupling in the liquid phase becomes less sensitive to temperature, consistent with earlier theoretical predictions of more stable coupling in metallic liquids [53].

Around 700–800 fs, G_{exp} is observed to be 10–20 % higher than $G_{cal}(\tau = 1.6\,\text{ps})$, suggesting a possible phase coexistence regime where solid and liquid domains coexist. Such spatial inhomogeneities could lead to averaging effects across regions with different coupling strengths and electronic properties, which are not captured by our spatially uniform model. This observation motivates future work incorporating phase-field modeling, inhomogeneous TTM frameworks, or molecular dynamics with spatial resolution.

5. Conclusion

In this study, we investigated electron-phonon and electron-ion coupling in warm dense copper using femtosecond time-resolved X-ray absorption near-edge structure (XANES) spectroscopy. By directly probing the transient evolution of the Cu L_3 edge with high temporal and spectral resolution, we extracted the time-dependent energy transfer rates from the electronic subsystem to the lattice across both solid and liquid phases. Our results demonstrate that nonthermal electron distributions significantly enhance the electron-phonon coupling strength in the solid phase. This enhancement originates from the broadened electron energy distribution immediately following ultrafast laser excitation, which increases the available phase space for electron-phonon scattering. As the system evolves, the lattice absorbs sufficient energy to induce melting, leading to a sharp decrease in the coupling strength. In the liquid phase, the coupling becomes weaker and more stable, exhibiting reduced sensitivity to both temperature and electron distribution shape. This behavior is consistent with the transition to a disordered atomic structure and a more thermalized electronic system.

These observations are quantitatively reproduced using a modified two-temperature model that incorporates nonequilibrium electron kinetics and density functional theory-based calculations of the electronic density of states. The combination of time-resolved spectroscopy

and advanced modeling provides benchmark data and a validated framework for studying energy relaxation processes in warm dense matter.

Our findings provide critical experimental validation and a refined theoretical understanding of nonequilibrium effects in warm dense copper. By explicitly incorporating nonequilibrium electron kinetics into our modeling framework, we demonstrate the necessity of considering transient electronic structures to accurately describe ultrafast energy transfer processes. Future studies may extend these insights through advanced theoretical approaches, including time-dependent DFT and spatially resolved models, to deepen our understanding of thermophysical properties and the complex phase-transition dynamics in warm dense matter at ultrafast timescales.

Acknowledgements

We would like to acknowledge the European XFEL in Schenefeld, Germany, for provision of X-ray free electron laser beamtime at the SCS instrument, and we thank the staff for their assistance. This work was supported by the Institute for Basic Science (IBS- R038-D1), the National Research Foundation of Korea (RS-2022-00207260, RS-2023-00218180, RS-2025-00516264, RS-2025-02318077), and the Korean Government MSIT (RS-2022-00164805, Accelerator Application Support Project). S.A. and S.M.V. acknowledge support from the UK EPSRC grant EP/W010097/1 and from the Royal Society.

Data Availability

Data recorded for the experiments at the European XFEL are available at DOI:10.22003/XFEL.EU-DATA-003216-00 and DOI:10.22003/XFEL.EU-DATA-002497-00. The processed XANES spectra and calculation codes are available on request to corresponding author.

Declaration of Competing Interest

The authors declare that they have no known competing financial interest or personal relationships that could have appeared to influence the work reported in this paper.

Keywords

Laser-matter interaction, Ultrafast melting, Warm dense matter, X-ray absorption near-edge structure, Electron-phonon coupling

Reference

[1] A. Ng, T. Ao, F. Perrot, M.W.C. Dharma-Wardana, M.E. Foord, Idealized slab plasma approach for the study of warm dense matter, Laser and Particle Beams, 23 (2005) 527-537.

[2] Y. Ping, A.A. Correa, T. Ogitsu, E. Draeger, E. Schwegler, T. Ao, K. Widmann, D.F. Price, E. Lee, H. Tam, P.T. Springer, D. Hanson, I. Koslow, D. Prendergast, G. Collins, A. Ng, Warm dense matter created by isochoric laser heating, High Energy Density Physics, 6 (2010) 246-257.

[3] Z. Chen, B. Holst, S.E. Kirkwood, V. Sametoglu, M. Reid, Y.Y. Tsui, V. Recoules, A. Ng, Evolution of ac Conductivity in Nonequilibrium Warm Dense Gold, Physical Review Letters, 110 (2013) 135001.

[4] M. Kim, J.H. Jung, S.H. Yang, M.S. Cho, G. Kang, G. Lee, J.-W. Lee, S. Lee, J. Sohn, B.I. Cho, Effect of hot electron kinetics on self-reflectivity of warm dense gold irradiated with femtosecond laser pulses, Applied Surface Science, 561 (2021) 150073.

[5] R.W. Lee, H.A. Baldis, R.C. Cauble, O.L. Landen, J.S. Wark, A. Ng, S.J. Rose, C. Lewis, D. Riley, J.C. Gauthier, P. Audebert, Plasma-based studies with intense X-ray and particle beam sources, Laser and Particle Beams, 20 (2002) 527-536.

[6] A.J. Nelson, J. Dunn, J. Hunter, K. Widmann, Time-resolved x-ray laser induced photoelectron spectroscopy of isochoric heated copper, Applied Physics Letters, 87 (2005).

[7] R.W. Lee, S.J. Moon, H.-K. Chung, W. Rozmus, H.A. Baldis, G. Gregori, R.C. Cauble, O.L. Landen, J.S. Wark, A. Ng, S.J. Rose, C.L. Lewis, D. Riley, J.-C. Gauthier, P. Audebert, Finite temperature dense matter studies on next-generation light sources, J. Opt. Soc. Am. B, 20 (2003) 770-778.

[8] N. Booth, A.P.L. Robinson, P. Hakel, R.J. Clarke, R.J. Dance, D. Doria, L.A. Gizzi, G. Gregori, P. Koester, L. Labate, T. Levato, B. Li, M. Makita, R.C. Mancini, J. Pasley, P.P. Rajeev, D. Riley, E. Wagenaars, J.N. Waugh, N.C. Woolsey, Laboratory measurements of resistivity in warm dense plasmas relevant to the microphysics of brown dwarfs, Nature Communications, 6 (2015) 8742.

[9] S.H. Glenzer, B.J. MacGowan, P. Michel, N.B. Meezan, L.J. Suter, S.N. Dixit, J.L. Kline, G.A. Kyrala, D.K. Bradley, D.A. Callahan, E.L. Dewald, L. Divol, E. Dzenitis, M.J. Edwards, A.V. Hamza, C.A. Haynam, D.E. Hinkel, D.H. Kalantar, J.D. Kilkenny, O.L. Landen, J.D. Lindl, S. LePape, J.D. Moody, A. Nikroo, T. Parham, M.B. Schneider, R.P.J. Town, P. Wegner, K. Widmann, P. Whitman, B.K.F. Young, B. Van Wonterghem, L.J. Atherton, E.I. Moses, Symmetric Inertial Confinement Fusion Implosions at Ultra-High Laser Energies, Science, 327 (2010) 1228-1231.

[10] R. Torchio, F. Occelli, O. Mathon, A. Sollier, E. Lescoute, L. Videau, T. Vinci, A. Benuzzi-Mounaix, J. Headspith, W. Helsby, S. Bland, D. Eakins, D. Chapman, S. Pascarelli, P. Loubeyre, Probing local and electronic structure in Warm Dense Matter: single pulse synchrotron x-ray absorption spectroscopy on shocked Fe, Scientific Reports, 6 (2016) 26402.

[11] S.Y. Wang, Y. Ren, C.W. Cheng, J.K. Chen, D.Y. Tzou, Micromachining of copper by femtosecond laser pulses, Applied Surface Science, 265 (2013) 302-308.

[12] A. Ng, Outstanding questions in electron–ion energy relaxation, lattice stability, and dielectric function of warm dense matter, International Journal of Quantum Chemistry, 112 (2012) 150-160.

[13] T.G. White, J. Vorberger, C.R.D. Brown, B.J.B. Crowley, P. Davis, S.H. Glenzer, J.W.O. Harris, D.C. Hochhaus, S. Le Pape, T. Ma, C.D. Murphy, P. Neumayer, L.K.

Pattison, S. Richardson, D.O. Gericke, G. Gregori, Observation of inhibited electron-ion coupling in strongly heated graphite, Scientific Reports, 2 (2012) 889.
[14] J. Vorberger, D.O. Gericke, T. Bornath, M. Schlanges, Energy relaxation in dense, strongly coupled two-temperature plasmas, Physical Review E, 81 (2010) 046404.
[15] B.I. Cho, T. Ogitsu, K. Engelhorn, A.A. Correa, Y. Ping, J.W. Lee, L.J. Bae, D. Prendergast, R.W. Falcone, P.A. Heimann, Measurement of Electron-Ion Relaxation in Warm Dense Copper, Scientific Reports, 6 (2016) 18843.
[16] M.Z. Mo, Z. Chen, R.K. Li, M. Dunning, B.B.L. Witte, J.K. Baldwin, L.B. Fletcher, J.B. Kim, A. Ng, R. Redmer, A.H. Reid, P. Shekhar, X.Z. Shen, M. Shen, K. Sokolowski-Tinten, Y.Y. Tsui, Y.Q. Wang, Q. Zheng, X.J. Wang, S.H. Glenzer, Heterogeneous to homogeneous melting transition visualized with ultrafast electron diffraction, Science, 360 (2018) 1451-1455.
[17] J.-W. Lee, M. Kim, G. Kang, S.M. Vinko, L. Bae, M.S. Cho, H.-K. Chung, M. Kim, S. Kwon, G. Lee, C.H. Nam, S.H. Park, J.H. Sohn, S.H. Yang, U. Zastrau, B.I. Cho, Investigation of Nonequilibrium Electronic Dynamics of Warm Dense Copper with Femtosecond X-Ray Absorption Spectroscopy, Physical Review Letters, 127 (2021) 175003.
[18] L. Mercadier, A. Benediktovitch, Š. Krušič, J.J. Kas, J. Schlappa, M. Agåker, R. Carley, G. Fazio, N. Gerasimova, Y.Y. Kim, L. Le Guyader, G. Mercurio, S. Parchenko, J.J. Rehr, J.-E. Rubensson, S. Serkez, M. Stransky, M. Teichmann, Z. Yin, M. Žitnik, A. Scherz, B. Ziaja, N. Rohringer, Transient absorption of warm dense matter created by an X-ray free-electron laser, Nature Physics, (2024).
[19] N. Jourdain, L. Lecherbourg, V. Recoules, P. Renaudin, F. Dorchies, Electron-ion thermal equilibration dynamics in femtosecond heated warm dense copper, Physical Review B, 97 (2018) 075148.
[20] N. Jourdain, L. Lecherbourg, V. Recoules, P. Renaudin, F. Dorchies, Ultrafast Thermal Melting in Nonequilibrium Warm Dense Copper, Physical Review Letters, 126 (2021) 065001.
[21] K. Eidmann, J. Meyer-ter-Vehn, T. Schlegel, S. Hüller, Hydrodynamic simulation of subpicosecond laser interaction with solid-density matter, Physical Review E, 62 (2000) 1202-1214.
[22] G.M. Petrov, A. Davidson, D. Gordon, J. Peñano, Modeling of short-pulse laser-metal interactions in the warm dense matter regime using the two-temperature model, Physical Review E, 103 (2021) 033204.
[23] Z. Lin, L.V. Zhigilei, V. Celli, Electron-phonon coupling and electron heat capacity of metals under conditions of strong electron-phonon nonequilibrium, Physical Review B, 77 (2008) 075133.
[24] N.A. Smirnov, Copper, gold, and platinum under femtosecond irradiation: Results of first-principles calculations, Physical Review B, 101 (2020) 094103.
[25] J. Zhang, R. Qin, W. Zhu, J. Vorberger, Energy Relaxation and Electron-Phonon Coupling in Laser-Excited Metals, in: Materials, 2022.
[26] P. Ji, Y. Zhang, Ab initio determination of effective electron–phonon coupling factor in copper, Physics Letters A, 380 (2016) 1551-1555.
[27] K.P. Migdal, D.K. Il'nitsky, Y.V. Petrov, N.A. Inogamov, Equations of state, energy transport and two-temperature hydrodynamic simulations for femtosecond laser irradiated copper and gold, Journal of Physics: Conference Series, 653 (2015) 012086.
[28] A.M. Brown, R. Sundararaman, P. Narang, W.A. Goddard, H.A. Atwater, Ab initio phonon coupling and optical response of hot electrons in plasmonic metals, Physical Review B, 94 (2016) 075120.

[29] J. Winter, S. Rapp, M. Schmidt, H.P. Huber, Ultrafast laser processing of copper: A comparative study of experimental and simulated transient optical properties, Applied Surface Science, 417 (2017) 2-15.
[30] N. Medvedev, I. Milov, Contribution of inter- and intraband transitions into electron–phonon coupling in metals, The European Physical Journal D, 75 (2021) 212.
[31] G.M. Petrov, A. Davidson, Collisional and transport parameters of Cu in the warm dense matter regime calculated using the average atom model, Plasma Physics and Controlled Fusion, 63 (2021) 125011.
[32] L. Le Guyader, A. Eschenlohr, M. Beye, W. Schlotter, F. Doring, C. Carinan, D. Hickin, N. Agarwal, C. Boeglin, U. Bovensiepen, J. Buck, R. Carley, A. Castoldi, A. D'Elia, J.-T. Delitz, W. Ehsan, R. Engel, F. Erdinger, H. Fangohr, P. Fischer, C. Fiorini, A. Fohlisch, L. Gelisio, M. Gensch, N. Gerasimova, R. Gort, K. Hansen, S. Hauf, M. Izquierdo, E. Jal, E. Kamil, L. Kammerer, S. Karabekyan, T. Kluyver, T. Laarmann, T. Lojewski, D. Lomidze, S. Maffessanti, T. Mamyrbayev, A. Marcelli, L. Mercadier, G. Mercurio, P.S. Miedema, K. Ollefs, K. Rossnagel, B. Rosner, N. Rothenbach, A. Samartsev, J. Schlappa, K. Setoodehnia, G. Sorin Chiuzbaian, C. Stamm, F. Stellato, S. Techert, M. Teichmann, M. Turcato, B. Van Kuiken, H. Wende, A. Yaroslavtsev, J. Zhu, S. Molodtsov, C. David, M. Porro, A. Scherz, Photon-shot-noise-limited transient absorption soft X-ray spectroscopy at the European XFEL, Journal of Synchrotron Radiation, 30 (2023) 284-300.
[33] M. Porro, L. Andricek, S. Aschauer, A. Castoldi, M. Donato, J. Engelke, F. Erdinger, C. Fiorini, P. Fischer, H. Graafsma, A. Grande, C. Guazzoni, K. Hansen, S. Hauf, P. Kalavakuru, H. Klaer, M. Tangl, A. Kugel, M. Kuster, P. Lechner, D. Lomidze, S. Maffessanti, M. Manghisoni, S. Nidhi, F. Okrent, V. Re, C. Reckleben, E. Riceputi, R. Richter, A. Samartsev, S. Schlee, J. Soldat, L. Strüder, J. Szymanski, M. Turcato, G. Weidenspointner, C.B. Wunderer, The MiniSDD-Based 1-Mpixel Camera of the DSSC Project for the European XFEL, IEEE Transactions on Nuclear Science, 68 (2021) 1334-1350.
[34] E. Bévillon, J.P. Colombier, V. Recoules, R. Stoian, Free-electron properties of metals under ultrafast laser-induced electron-phonon nonequilibrium: A first-principles study, Physical Review B, 89 (2014) 115117.
[35] B.I. Cho, K. Engelhorn, A.A. Correa, T. Ogitsu, C.P. Weber, H.J. Lee, J. Feng, P.A. Ni, Y. Ping, A.J. Nelson, D. Prendergast, R.W. Lee, R.W. Falcone, P.A. Heimann, Electronic Structure of Warm Dense Copper Studied by Ultrafast X-Ray Absorption Spectroscopy, Physical Review Letters, 106 (2011) 167601.
[36] B. Mahieu, N. Jourdain, K. Ta Phuoc, F. Dorchies, J.P. Goddet, A. Lifschitz, P. Renaudin, L. Lecherbourg, Probing warm dense matter using femtosecond X-ray absorption spectroscopy with a laser-produced betatron source, Nature Communications, 9 (2018) 3276.
[37] X. Zhang, B. Grabowski, F. Körmann, C. Freysoldt, J. Neugebauer, Accurate electronic free energies of the 3*d*,4*d*, and 5*d* transition metals at high temperatures, Physical Review B, 95 (2017) 165126.
[38] P. Giannozzi, O. Andreussi, T. Brumme, O. Bunau, M. Buongiorno Nardelli, M. Calandra, R. Car, C. Cavazzoni, D. Ceresoli, M. Cococcioni, N. Colonna, I. Carnimeo, A. Dal Corso, S. de Gironcoli, P. Delugas, R.A. DiStasio, A. Ferretti, A. Floris, G. Fratesi, G. Fugallo, R. Gebauer, U. Gerstmann, F. Giustino, T. Gorni, J. Jia, M. Kawamura, H.Y. Ko, A. Kokalj, E. Küçükbenli, M. Lazzeri, M. Marsili, N. Marzari, F. Mauri, N.L. Nguyen, H.V. Nguyen, A. Otero-de-la-Roza, L. Paulatto, S. Poncé, D. Rocca, R. Sabatini, B. Santra, M. Schlipf, A.P. Seitsonen, A. Smogunov, I. Timrov, T. Thonhauser, P. Umari, N. Vast, X. Wu, S. Baroni, Advanced capabilities for materials

modelling with Quantum ESPRESSO, Journal of Physics: Condensed Matter, 29 (2017) 465901.
[39] M.J. van Setten, M. Giantomassi, E. Bousquet, M.J. Verstraete, D.R. Hamann, X. Gonze, G.M. Rignanese, The PseudoDojo: Training and grading a 85 element optimized norm-conserving pseudopotential table, Computer Physics Communications, 226 (2018) 39-54.
[40] D.R. Hamann, Optimized norm-conserving Vanderbilt pseudopotentials, Physical Review B, 88 (2013) 085117.
[41] J.P. Perdew, K. Burke, M. Ernzerhof, Generalized Gradient Approximation Made Simple, Physical Review Letters, 77 (1996) 3865-3868.
[42] H.J. Monkhorst, J.D. Pack, Special points for Brillouin-zone integrations, Physical Review B, 13 (1976) 5188-5192.
[43] E. Carpene, Ultrafast laser irradiation of metals: Beyond the two-temperature model, Physical Review B, 74 (2006) 024301.
[44] M. Uehlein, S.T. Weber, B. Rethfeld, Influence of Electronic Non-Equilibrium on Energy Distribution and Dissipation in Aluminum Studied with an Extended Two-Temperature Model, Nanomaterials, 12 (2022) 1655.
[45] G.D. Tsibidis, Ultrafast dynamics of non-equilibrium electrons and strain generation under femtosecond laser irradiation of Nickel, Applied Physics A, 124 (2018) 311.
[46] T. Held, S.T. Weber, B. Rethfeld, Influence of band occupation on electron-phonon coupling in gold, Journal of Physics: Condensed Matter, 37 (2025) 095001.
[47] H. Ebert, J. Stöhr, S.S.P. Parkin, M. Samant, A. Nilsson, L-edge x-ray absorption in fcc and bcc Cu metal: Comparison of experimental and first-principles theoretical results, Physical Review B, 53 (1996) 16067-16073.
[48] O. Bunău, M. Calandra, Projector augmented wave calculation of x-ray absorption spectra at the $L_{2,3}$ edges, Physical Review B, 87 (2013) 205105.
[49] H.E. Elsayed-Ali, T.B. Norris, M.A. Pessot, G.A. Mourou, Time-resolved observation of electron-phonon relaxation in copper, Physical Review Letters, 58 (1987) 1212-1215.
[50] J.M. Ziman, Electrons and Phonons, Oxfort University Press, London, 1960.
[51] P.B. Allen, Theory of thermal relaxation of electrons in metals, Physical Review Letters, 59 (1987) 1460-1463.
[52] X.Y. Wang, D.M. Riffe, Y.S. Lee, M.C. Downer, Time-resolved electron-temperature measurement in a highly excited gold target using femtosecond thermionic emission, Physical Review B, 50 (1994) 8016-8019.
[53] J. Simoni, J. Daligault, First-Principles Determination of Electron-Ion Couplings in the Warm Dense Matter Regime, Physical Review Letters, 122 (2019) 205001.